

# UCLA

## UCLA Previously Published Works

### Title

Stretchable [2]rotaxane-bridged MXene films applicable for electroluminescent devices.

### Permalink

<https://escholarship.org/uc/item/1hn1h669>

### Journal

Science Advances, 11(10)

### Authors

Wang, Chunyu

Gao, Boyue

Xue, Kai

et al.

### Publication Date

2025-03-07

### DOI

10.1126/sciadv.adt8262

Peer reviewed

## CHEMISTRY

## Stretchable [2]rotaxane-bridged MXene films applicable for electroluminescent devices

Chunyu Wang<sup>1,2†</sup>, Boyue Gao<sup>1,3†</sup>, Kai Xue<sup>1,3</sup>, Wenbin Wang<sup>1,2</sup>, Jun Zhao<sup>1,2</sup>, Ruixue Bai<sup>1,2</sup>, Tinghao Yun<sup>1,2</sup>, Zhiwei Fan<sup>1,2</sup>, Mengling Yang<sup>1,2</sup>, Zhaoming Zhang<sup>1,2</sup>, Zhitao Zhang<sup>1,3\*</sup>, Xuzhou Yan<sup>1,2\*</sup>

Titanium carbide ( $\text{Ti}_3\text{C}_2\text{T}_x$ ) MXene has prominent mechanical properties and electrical conductivity. However, fabricating high-performance macroscopic films is challenging, as weak interlayer interactions limit their mechanical performance. Here, we introduce [2]rotaxane, a mechanically interlocked molecule, to enhance MXene films. Compared to pure MXene (fracture strain: 4.6%, toughness: 0.6 MJ/m<sup>3</sup>), [2]rotaxane-bridged MXene (RBM) films achieve record-high strain (20.0%) and toughness (11.9 MJ/m<sup>3</sup>) with only 3.6% [2]rotaxane by weight. Additionally, RBM films endure 500 stretch cycles (0 to 15% strain) with stable and reversible resistance alterations, making them ideal for stretchable electrodes. Notably, RBM films enable stretchable electroluminescent devices with reliable operation under 20% elongation and customizable luminescent patterns. This innovative use of mechanically interlocked molecules to cross-link MXene platelets advances MXene films and other two-dimensional materials in stretchable electronics.

## INTRODUCTION

Titanium carbide ( $\text{Ti}_3\text{C}_2\text{T}_x$ ) MXene stands out as a promising two-dimensional material, capturing widespread interest since its discovery in 2011 (1). Its remarkable electrical conductivity and mechanical performance make it a frontrunner in various domains such as flexible electronics (2, 3), supercapacitors (4, 5), batteries (6), sensors (7), and electromagnetic interference shielding (8, 9), among many others. However, transforming MXene platelets into high-performance macroscopic films is hindered because of their inherent fragility and lack of malleability. To address this challenge, researchers have turned to interlayer interactions, including hydrogen bonding (10, 11), ionic bonding (12, 13), and covalent bonding (14, 15), enabled by abundant functional groups (—OH, —F, and =O) on the surface of MXene platelets. For example, by using hydrogen bonding, MXene-sodium carboxymethyl cellulose and MXene-sodium alginate hybrid films have been fortified (16, 17), while aluminum ion- and calcium ion-reinforced MXene films have been fabricated relying on ionic bonding (17, 18). Although these advancements have bolstered the tensile strength of MXene films, achieving notable elongation remains difficult, particularly with additive contents limited to 5% by weight. As is well known, the elongation of materials plays a pivotal role in the field of flexible and stretchable electronics (19, 20). A high degree of elongation allows materials to retain original properties under various strains, such as tension, torsion, and shear, without succumbing to severe material failure. For bulk MXene films, nevertheless, achieving both high stretchability and stable electrical conductivity is still a major challenge, impeding progress in flexible and stretchable electronics. Despite its importance, stretchability often takes a backseat in the development of MXene films as well as maintaining

conductivity during the strain process, highlighting the need for further research.

Mechanically interlocked molecules, such as rotaxanes, catenanes, and molecular knots, are spatially entangled molecular architectures valued for their special intramolecular motion properties, including sliding, circumrotation, and translation (21–25). The involved interlocked components are connected by mechanical bonding instead of covalent bonding, but the mechanical strength of mechanical bonding was found to be comparable to that of covalent bonding (26, 27). [2]Rotaxane represents a typical class of mechanically interlocked molecules, where one wheel molecule is threaded through one dumbbell-shaped axle molecule (28–31). Once stimulated by external force, the wheel molecule can slide along the axle to release the hidden chain, while the stoppers prevent it from sliding off. Hence, the special intramolecular sliding motion imparts dynamic stability and mechanical adaptivity to [2]rotaxane. Drawing inspiration from this behavior, we propose to incorporate [2]rotaxane into MXene films to improve the latter mechanical performance by making use of the intramolecular sliding motion to retard the slip-off between MXene platelets. This perspective may offer a promising strategy for advancing MXene films in the realms of flexible and stretchable electronics. To the best of our knowledge, the use of [2]rotaxane for toughening and strengthening MXene films has not yet been explored.

Here, we report a stretchable and tough [2]rotaxane-bridged MXene (RBM) film, of which the intramolecular sliding of [2]rotaxane releases the hidden chain, thereby increasing the slip distance between MXene platelets (Fig. 1, A and B). Accordingly, the stretchability and toughness of RBM films make them suitable for use as electrodes in stretchable and patternable alternating current electroluminescent (ACEL) devices (Fig. 1C). In particular, covalent carbonate ester linkage was created to cross-link [2]rotaxane and MXene films, thus to afford RBM films. Impressively, the RBM films exhibited greatly enhanced mechanical properties, particularly the fracture strain (20.0%) and toughness (11.9 MJ/m<sup>3</sup>) reaching a record high. Moreover, RBM films showcased a quality of conductivity uniformity during cyclic

Copyright © 2025 The Authors, some rights reserved; exclusive licensee American Association for the Advancement of Science. No claim to original U.S. Government Works. Distributed under a Creative Commons Attribution NonCommercial License 4.0 (CC BY-NC).

<sup>1</sup>School of Chemistry and Chemical Engineering, Shanghai Jiao Tong University, Shanghai, China. <sup>2</sup>Frontiers Science Center for Transformative Molecules, Shanghai Jiao Tong University, Shanghai, China. <sup>3</sup>Zhangjiang Institute for Advanced Study, Shanghai Jiao Tong University, Shanghai, China.

\*Corresponding author. Email: zhangzhitao@sjtu.edu.cn (Zhitao Zhang); xzyan@sjtu.edu.cn (X.Y.)

†These authors contributed equally to this work.

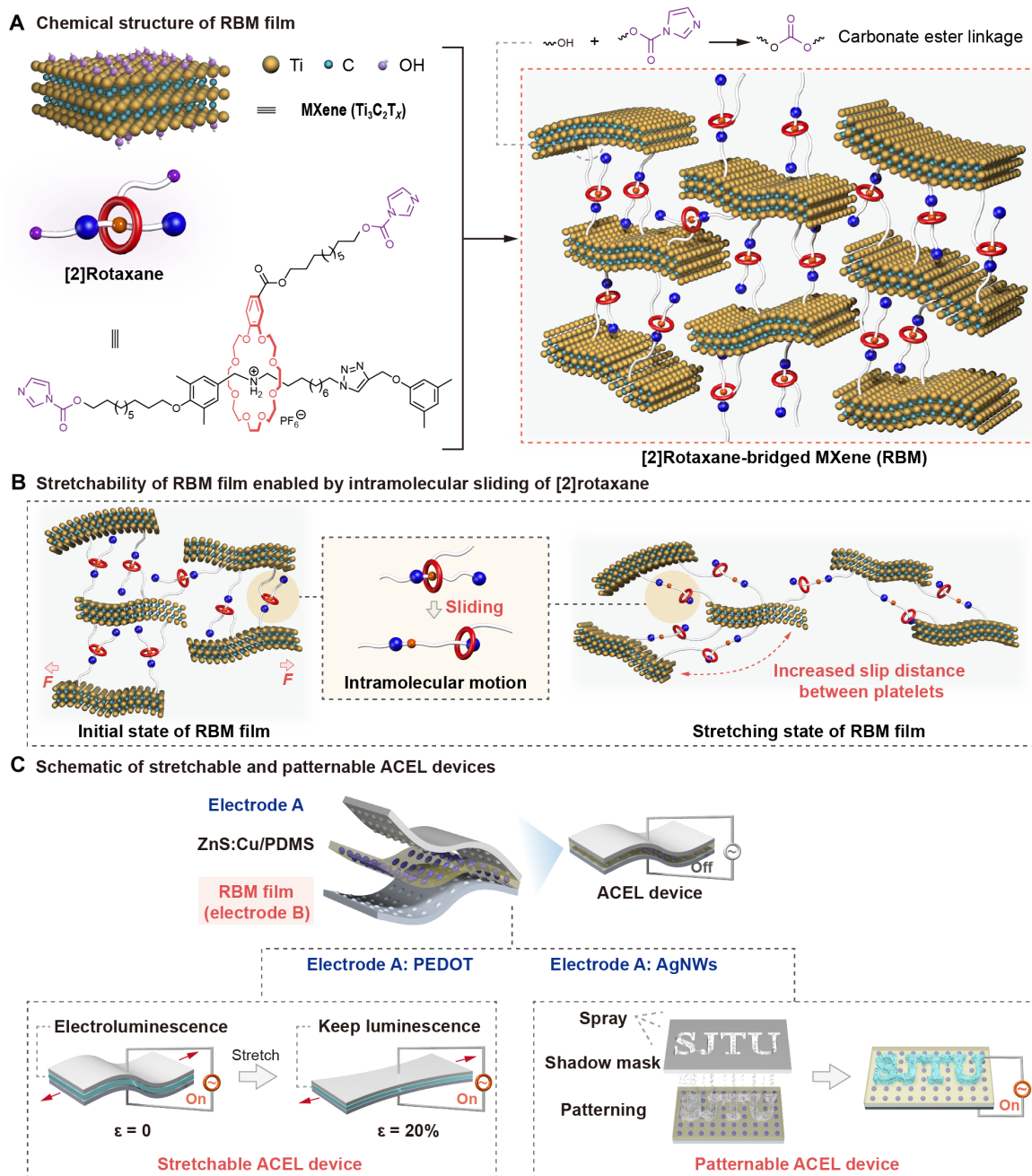


**Fig. 1. Cartoon representation for the structure diagram of RBM film, the toughening mechanism of [2]rotaxane, and an overall stretchable and patternable ACEL device schematic.** (A) Cartoon representation for MXene films bridged by [2]rotaxane and the structures of MXene and [2]rotaxane cross-linker. (B) The toughening mechanism is speculated that the hidden chain of [2]rotaxane is released due to intramolecular mechanical motion under external force, resulting in an increased interlayer slip distance between MXene platelets. (C) The ACEL devices consist of three layers including the top electrode (PEDOT or AgNWs), the middle emissive layer (ZnS:Cu/PDMS), and the bottom electrode (RBM film), in which the electroluminescence is excited under alternating current and is maintained even when the device is stretched to 20% strain or patterned to SJTU letters.

stretching between 0 and 15% strain, which ensured that the electric field intensity applied to the RBM films could be maintained at high voltage throughout the stretching process. These characteristics collectively positioned RBM films as a highly promising candidate for stretchable electrodes in ACEL devices. As a result, RBM films steadily actuated ACEL devices under elongations of up to 20%, delivering high brightness, uniform blue light emission, and patternability.

## RESULTS

### Synthesis and structural characterization of [2]rotaxane

As mentioned previously, the surface functional groups, especially  $-\text{OH}$ , facilitate interfacial interactions between MXene platelets when specific additives are introduced.  $N,N'$ -carbonyldiimidazole (CDI), known for its strong reactivity, can react with two moles of  $-\text{OH}$  to form a carbonate ester linkage (32, 33). Motivated by this reactivity,

we aimed to use CDI to tightly couple MXene and [2]rotaxane. To this end, we firstly synthesized [2]rotaxane with terminal —OH groups based on our previous work (30). Before cross-linking [2]rotaxane and MXene, CDI was allowed to react with [2]rotaxane, replacing the hydrogen atom of —OH with a carbonyl imidazole unit, denoted as [2]rotaxane-CDI (see Materials and Methods). The structure of the resulting [2]rotaxane-CDI was confirmed using a hydrogen nuclear magnetic resonance ( $^1\text{H}$  NMR) spectrum (Fig. 2). Compared with [2]rotaxane-OH, the three emerging signals of  $\text{H}^\alpha$ ,  $\text{H}^\beta$ , and  $\text{H}^\gamma$  derived from carbonyl imidazole unit were detected in the  $^1\text{H}$  NMR spectrum of [2]rotaxane-CDI. Besides,  $\text{H}^5$  and  $\text{H}^e$  shifted from upfield to downfield due to the stronger electron-withdrawing effect of carbonyl imidazole unit than hydrogen atom. A high-resolution mass spectrum further validated the structure of [2]rotaxane-CDI (fig. S4). Subsequent reactions involved [2]rotaxane-CDI coupling with —OH on MXene platelets, forming covalent carbonate ester linkage. To better illustrate the toughening effect of [2]rotaxane on MXene films, heptaethylene glycol-bridged MXene (HBM) films were prepared as control alongside pure MXene films, and the relevant content can be found in Materials and Methods.

### Design and structural characterizations of macroscopic films

MXene was prepared through etching  $\text{Ti}_3\text{AlC}_2$  to remove the Al layer following a minimally intensive layer delamination (MILD) method

(34), as depicted in Materials and Methods. X-ray diffraction (XRD) spectra (Fig. 3A) verified the successful preparation of MXene, as evidenced by the disappearance of the (104) peak at around  $39^\circ$  which indicated the elimination of Al element owing to the etching process (35, 36). Besides, the (002) characteristic peak became more prominent, and the corresponding  $2\theta$  shifted from  $9.5^\circ$  in  $\text{Ti}_3\text{AlC}_2$  to  $5.9^\circ$  in  $\text{Ti}_3\text{C}_2\text{T}_x$ . Atomic force microscope (AFM) measurements revealed that the thickness of the obtained MXene platelets in this work was approximately 2.2 nm (Fig. 3B). Next, MXene films were acquired through vacuum filtration of MXene dispersion solution on hydrophilic filter membranes followed by natural drying. These films were then immersed in *N,N*-dimethylformamide solution containing either [2]rotaxane-CDI or heptaethylene glycol-CDI. Thereafter, RBM and HBM films were obtained by a series of posttreatment, detailed in Materials and Methods.

The as-prepared RBM film was physically flexible and could be flexed using a tweezer (fig. S9). Scanning electron microscope (SEM) observation of RBM film cross section displayed a lamellar morphology because of the layer-by-layer assembly of MXene platelets (Fig. 3C). According to energy dispersive x-ray spectra, the distribution of N element was as uniform as that of Ti and C (Fig. 3C), confirming the incorporation of [2]rotaxanes into MXene films. The surface of pure MXene film was covered by —OH groups, which were replaced by [2]rotaxane and heptaethylene glycol in RBM and HBM,

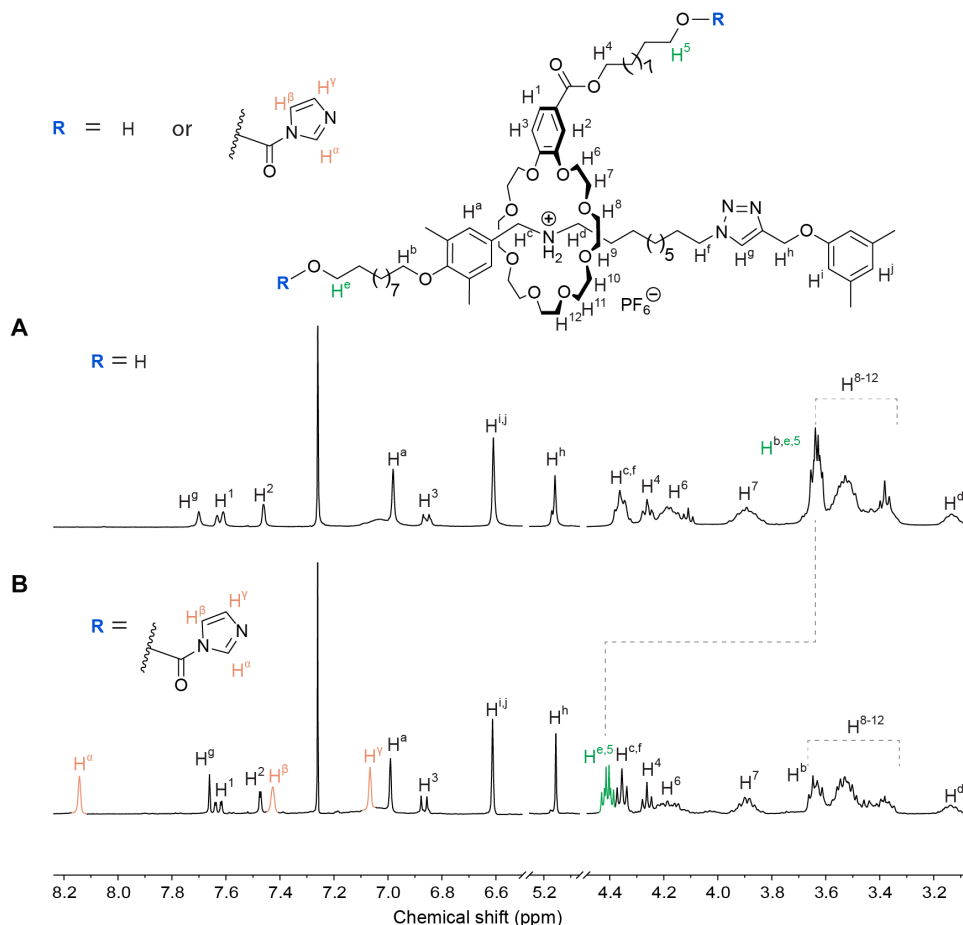


**Fig. 2. Structural characterization of [2]rotaxane.** Partial  $^1\text{H}$  NMR spectra ( $\text{CDCl}_3$ , 400 MHz, 298 K) of [2]rotaxane-OH (A) and [2]rotaxane-CDI (B). ppm, parts per million.

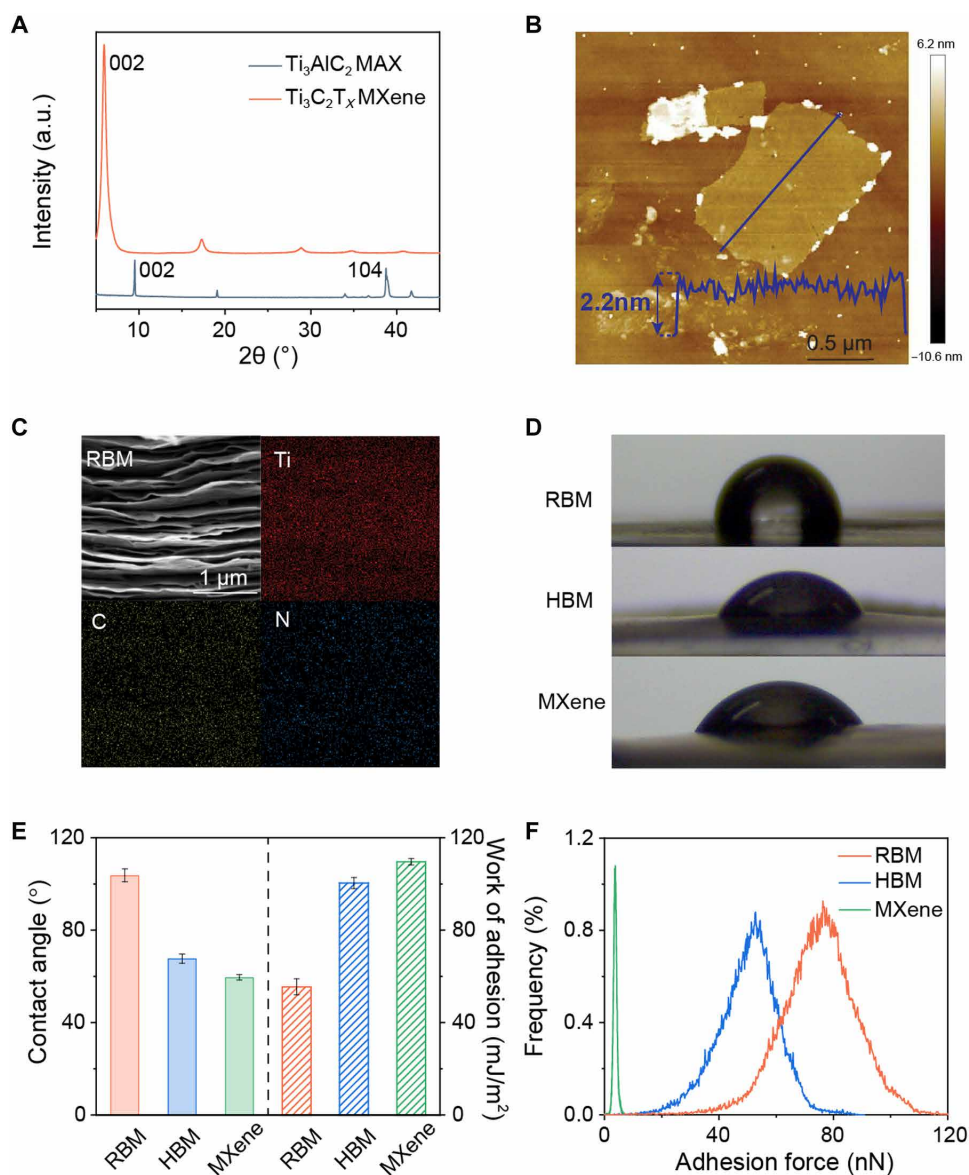


**Fig. 3. Micromorphology characterization of MXene platelets and RBM films and comparison of contact angle and adhesion force between RBM, HBM, and MXene films.** (A) XRD spectra of MXene ( $\text{Ti}_3\text{C}_2\text{T}_x$ ) and MAX ( $\text{Ti}_3\text{AlC}_2$ ). (B) AFM image of MXene platelets and the corresponding height profile. (C) The cross section of RBM film and elemental distribution mapping images of Ti, C, and N. (D) Images of contact angle for RBM, HBM, and pure MXene films. (E) Comparison of contact angle and work of adhesion between water and three films. (F) The distributions of AFM adhesion force for RBM, HBM, and pure MXene films. a.u., arbitrary units.

respectively. Therefore, we expected to roughly compare the surface difference of three films with the aid of contact angle measuring device (Fig. 3, D and E). Logically, the contact angle of MXene film was  $59.6^\circ$ , illustrating the hydrophilic nature of MXene owing to the abundant  $-\text{OH}$  groups. Heptaethylene glycol is water soluble, so the contact angle of HBM ( $67.7^\circ$ ) only had a small change compared with the pure MXene film. In contrast, [2]rotaxane is insoluble in water, so its existence resulted in hydrophobicity of RBM film with a contact angle of  $103.8^\circ$ . This phenomenon suggested that the [2]rotaxane successfully cross-linked MXene platelets, which changed the surface hydrophilicity of the films. Correspondingly, the works of adhesion between water and pure MXene, HBM, and RBM films were  $109.7$ ,  $100.4$ , and  $55.5$   $\text{mJ}/\text{m}^2$ , respectively, demonstrating that [2]rotaxane

greatly influenced the affinity of RBM film for water. In addition, the introduction of [2]rotaxane and heptaethylene glycol had an impact on the adhesion of the AFM tip when it tapped the film surface, and the mappings and corresponding distributions of the adhesion forces are showcased in Fig. 3F and fig. S10. The average adhesion force was  $3.8$  nN for the surface of pure MXene film, which was much lower than that of  $52.8$  nN for HBM film and  $76.3$  nN for RBM film. Obviously, [2]rotaxane and heptaethylene glycol imparted the film surface stronger adhesion force to the AFM tip than  $-\text{OH}$ . As for RBM film, the relatively large volume of [2]rotaxane may contribute to the resistance when AFM tip moved across the film surface. On the other hand, the increased molecular distance caused by the intramolecular sliding [2]rotaxane may also lead to the rise in the adhesion.

In Fig. 4A, XRD patterns show that the characteristic peaks for the three films were located at  $5.88^\circ$  (RBM),  $6.52^\circ$  (HBM), and  $6.01^\circ$  (MXene), and the corresponding interplanar spacing were 1.50 nm (RBM), 1.35 nm (HBM), and 1.47 nm (MXene) by calculation depending on Bragg equation (see the Supplementary Materials). Compared to pure MXene films, the shorter interplanar spacing for HBM films was associated with covalent bonding between heptaethylene glycol and MXene platelets. The interplanar spacing of films increased to 1.70 nm due to the expanded volume (fig. S11), if [2]rotaxane terminated with  $-\text{OH}$  was simply intercalated between MXene platelets rather than covalent cross-linking. In contrast, the interplanar spacing of RBM film presented only a slight increase than pure MXene film, indirectly illustrating the formation of covalent carbonate ester linkage between [2]rotaxanes and platelets. To further prove the presence of covalent carbonate ester linkage, we performed Fourier transform infrared (FTIR) tests, as shown in fig. S12. The FTIR spectrum of pure MXene film displayed a broad peak at around  $3480\text{ cm}^{-1}$  ascribed to the abundant  $-\text{OH}$  (16, 17), which however disappeared for that of RBM and HBM films because  $-\text{OH}$  participated in the reaction with [2]rotaxane-CDI and heptaethylene glycol-CDI. Correspondingly, an emerging peak at nearly  $1655\text{ cm}^{-1}$  appeared with the formation of  $-\text{COO}-$ , originating from carbonate ester linkage, in the FTIR spectra of RBM and HBM films (37). Moreover, the weight concentrations of [2]rotaxane and heptaethylene glycol accounting for RBM and HBM films were roughly estimated at 3.6 and 1.4%, respectively, by thermogravimetric analysis (TGA; Fig. 4B). According to wide sweep spectra of x-ray photoelectron spectroscopy (XPS; Fig. 4C), a distinct peak of  $\text{N}_{1s}$  at around 400-eV binding energy appeared in the RBM film spectrum, which was ascribed to secondary ammonium group and triazole unit of [2]rotaxane. Correspondingly, two peaks,  $\text{C}-\text{N}-\text{N}=\text{N}$  (399.9 eV) and  $\text{C}-\text{NH}_2^+$  (401.6 eV), were identified in the  $\text{N}_{1s}$  spectrum of RBM film (Fig.

4D) (38, 39). In the narrow sweep spectrum for  $\text{C}_{1s}$ , an additional peak ( $\text{C}-\text{N}$ ) at approximately 285.2 eV was differentiated for RBM films (40, 41), in addition to the four normal peaks,  $\text{C}-\text{Ti}$  (281.6 eV),  $\text{C}-\text{C}$  (284.6 eV),  $\text{C}-\text{O}$  (286.1 eV), and  $-\text{COO}-$  (288.7 eV) (16, 17), as depicted in Fig. 4E. Compared to pure MXene film, the  $\text{C}-\text{O}$  and  $-\text{COO}-$  peaks were downshifted for RBM and HBM films because of the generation of covalent carbonate ester linkage (Fig. 4E and fig. S13). Regarding the main  $\text{Ti}_{2p3/2}$  peak for RBM film, five peaks can be fitted,  $\text{Ti}-\text{C}$  (454.9 eV),  $\text{Ti}^{2+}$  (455.7 eV),  $\text{Ti}^{3+}$  (457.2 eV),  $\text{Ti}-\text{O}$  (458.8 eV), and  $\text{Ti}-\text{F}$  (459.8 eV) (42), as showcased in Fig. 4F. However, the introduction of [2]rotaxane and heptaethylene glycol did not cause obvious shift of  $\text{Ti}_{2p3/2}$  fitted peaks (Fig. 4F and fig. S13). Thus, the above XPS analyses revealed that [2]rotaxanes were successfully covalently cross-linked with MXene platelets.

### Mechanical performance of macroscopic films

The mechanical properties of pure MXene films are limited by the weak interlayer interactions, primarily hydrogen bonding, resulting in a tensile strength of  $19.0 \pm 0.18\text{ MPa}$ , a maximum strain of  $4.6 \pm 0.26\%$ , and a toughness of  $0.6 \pm 0.06\text{ MJ/m}^3$  (Fig. 5, A and B, and fig. S14). As is well known, MXene films are assembled through the lamellar stacking of MXene platelets, indicating that the fracture of MXene films signifies the slip-off between lamellas, which can be mitigated by strengthening interlayer interactions. Therefore, [2]rotaxane was brought in to delay the separation of MXene platelets and consequently improve the mechanical properties of MXene films. [2]Rotaxane boasts a unique molecular structure comprising a wheel molecule and a dumbbell-shaped axle molecule. In the absence of external stimulus, the wheel remains at the secondary ammonium recognition site due to the host-guest interaction. However, under external force, host-guest interaction dissociates, allowing the wheel to slide along the axle, releasing a hidden chain and dissipating

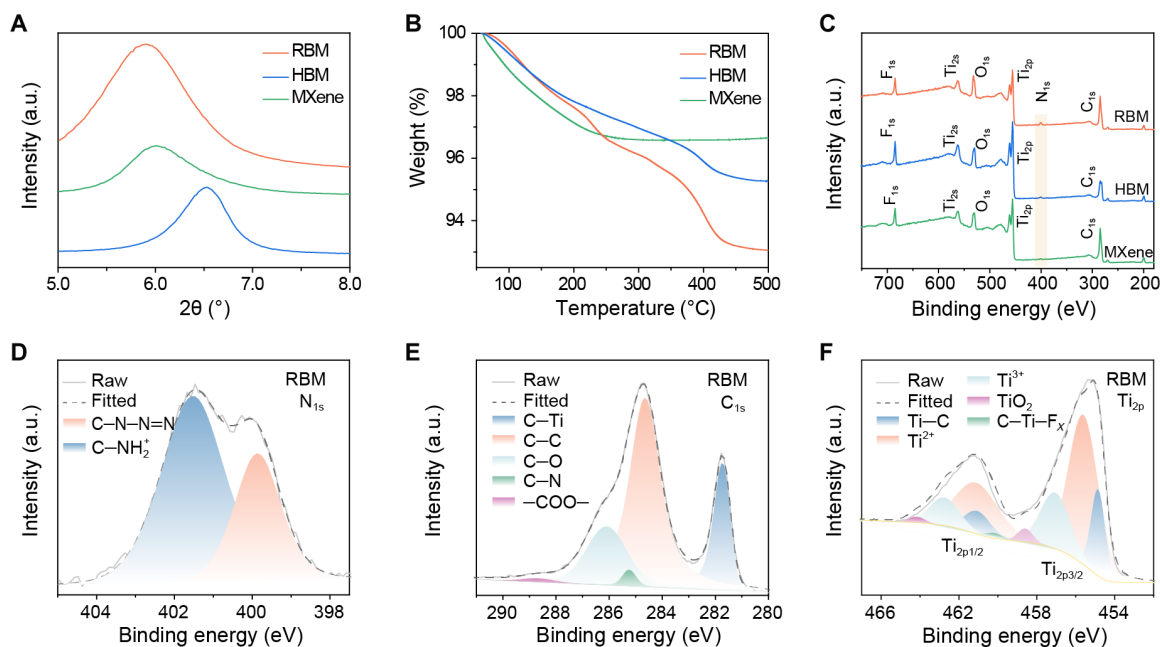


**Fig. 4. XRD, TGA, and XPS characterization of RBM, HBM, and MXene films.** (A) XRD patterns with  $2\theta$  ranging from  $5.0^\circ$  to  $8.0^\circ$  for RBM, HBM, and pure MXene films. (B) TGA curves for three films, conducted under nitrogen atmosphere from  $50^\circ$  to  $450^\circ\text{C}$  using a temperature rise rate of  $20^\circ\text{C}/\text{min}$ . (C) XPS spectra for three films between 200 and 750 eV. The specific XPS spectra for  $\text{N}_{1s}$  (D),  $\text{C}_{1s}$  (E), and  $\text{Ti}_{2p}$  (F) of RBM films.

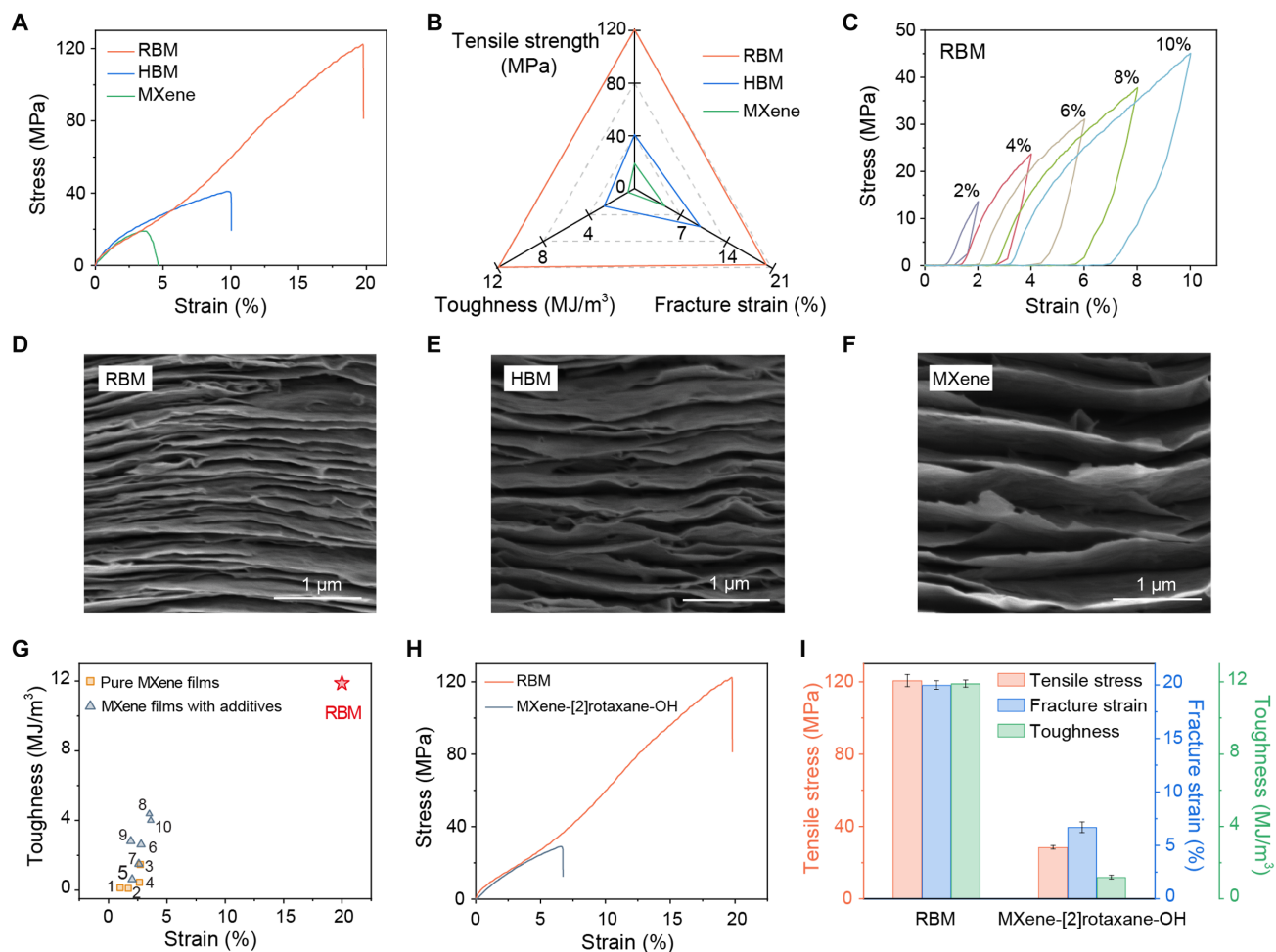


**Fig. 5. Mechanical properties of RBM films and corresponding comparison with other films.** (A) Typical stress-strain curves for RBM, HBM, and pure MXene films. (B) Comparison of the tensile strength, fracture strain, and toughness for three films. (C) Cyclic tensile test curves of RBM films with increased maximum strains. The cross-sectional SEM images of RBM (D), HBM (E), and pure MXene (F) films after tensile fractures. (G) Comparison of the tensile strain and toughness of the RBM films with those of previously reported MXene films with additives less than 5 wt %. The references correlated with the sample numbers in this chart are summarized in table S2. (H) Typical stress-strain curves for RBM and MXene-[2]rotaxane-OH films. (I) Comparison of the tensile strength, fracture strain, and toughness for RBM and MXene-[2]rotaxane-OH films.

energy, as illustrated in Fig. 1B. As such, this distinctive property enabled [2]rotaxane to postpone film fracture caused by slippage among platelets. As a result, RBM films achieved a tensile strength of  $120.7 \pm 3.3$  MPa, a maximum strain of  $20.0 \pm 0.4\%$ , and a toughness of  $11.9 \pm 0.2$  MJ/m<sup>3</sup> with only 3.6% [2]rotaxane by weight, which are 6.4, 4.3, and 19.8 times, respectively, higher than those observed for pure MXene film. Notably, the maximum strain and toughness of the RBM films set a record-high up to now with respect to those MXene films with less than 5% additives by weight, as presented in Fig. 5G. Although introducing heptaethylene glycol to cross-link MXene platelets also improved the mechanical properties of HBM films, the impact was limited due to its inability to perform intramolecular motion (Fig. 5, A and B, and fig. S14).

In addition, cyclic tensile tests were conducted on RBM film to discover that the cyclic tensile curves exhibited a regular pattern with a consistent increase in strain by 1% sequentially, as depicted in Fig. 5C and fig. S15. This behavior corresponds to the high fracture strain and further validates the good stretchability of RBM films. Moreover, the cross sections of the three films after being stretched to break were compared using SEM, as displayed in Fig. 5

(D to F). It was observed that the lamellar structure of RBM films was the most compact, followed by HBM films, whereas pure MXene films exhibited a rather loose lamellar cross section. This phenomenon can relate to the tensile fracture mechanism. During stretching, slippage movement between layers occurred due to the layer stack-up pattern of platelets, so thereinto, the interlayer interactions alleviated the slippage until one layer was completely separated from the other. As pure MXene platelets were bridged by weak interfacial interactions (mainly hydrogen bonding), pure MXene films broke quickly once stretched, resulting in a loose lamellar arrangement after fracture. However, the presence of [2]rotaxane and heptaethylene glycol increased the slippage distance between adjacent nanosheets. Upon external force, these robust molecules would withstand the stretching tension between platelets until the film broke. In consequence, the platelets were densely stacked, contributing to the compact lamellar morphology. The key difference presumably lies in the release of hidden chains deriving from the intramolecular motion of [2]rotaxane, which generated longer slippage distance and stronger stretching tension, leading to the highest compactness observed in RBM films.

We also conducted an experiment to verify the importance of carbonate ester linkage through combining MXene film with [2]rotaxane-OH (denoted as MXene-[2]rotaxane-OH), namely, no CDI was involved. Compared with pure MXene film, the mechanical properties of MXene-[2]rotaxane-OH film were slightly improved, which can be attributed to the hydrogen bonding between —OH groups (Fig. 5, A and H). However, the hydrogen bonding was not as strong as the covalent carbonate ester bonding, resulting that MXene-[2]rotaxane-OH film exhibited inferior mechanical properties to that of RBM film (Fig. 5, H and I). This indicated that the simple incorporation of [2]rotaxane into MXene film without cross-linking was unavailing because the intramolecular motion of [2]rotaxane failed to function during the stretching of the film.

### Using the RBM film as a stretchable electrode for ACEL devices

The electrical conductivity of RBM and HBM films increased from 138.5 S/cm for pure MXene films to 198.4 and 217.8 S/cm, respectively. The enhancement can be attributed to the shorter interplanar spacing, which was more favorable to electrons transfer (16, 17). Combined with the elongation up to 20.0%, RBM films herein mastered a great potential for stretchable electrodes and stretchable capacitors (3, 43–46). To elucidate the alteration in the conductivity of the MXene film under stretching, tensile tests were conducted to determine the resistance variation (Fig. 6A). As the stretching process unfolded, the strain exerted a discernible effect on the resistance of the RBM film. Initially, the resistance declined to  $0.9R_0$  within the initial 5% strain. As the tensile process continued, the film resistance exhibited a gradual increase, reaching a maximum of  $1.26R_0$  at 20% strain. The observed variation in resistance with respect to the strain can be attributed to the interlayer distance of the RBM film. An increase in elongation to 5% resulted in a corresponding decrease in interlayer distance for the MXene layers, which in turn facilitated enhanced charge transfer between the layers and a reduction in the resistance of the RBM film. However, above a critical strain value of 10%, the slip distance between the MXene nanosheets began to increase, becoming the dominant factor affecting the change of resistance. This led to an increase in resistance for the RBM film. Furthermore, the long-term stability of the conductivity performance as a function of stretching was confirmed by means of cycling tests. As exhibited in Fig. 6B, the cyclic stretching tests conducted on the RBM film, spanning a range of 0 to 15% strain, demonstrated consistent and reversible resistance alterations over a minimum of 500 cycles. This indicated that the RBM film had decent stretchability, mechanical robustness, and stable conductivity during the stretching process. Therefore, the RBM film shows great promise for use in stretchable electronic devices.

Given the prominent mechanical stretchability and conductivity, RBM films were applied as the stretchable electrodes for ACEL devices. As illustrated in Fig. 6C, the ACEL devices comprise an emissive layer positioned between two conductive electrodes, namely, the RBM film and the poly(3,4-ethylenedioxythiophene) (PEDOT) film. The proposed combination ensured that all layers were stretchable, thereby creating a fully stretchable ACEL device. The emissive layer was prepared by mixing ZnS:Cu nanoparticles with PDMS and then heat curing the resulting mixture to form a stretchable EL composite layer. The emissive layer can be readily extended to 100% strain without fracturing, thereby guaranteeing the light-emitting capabilities of the ACEL device throughout the stretching procedure

(47–49). The stretchability of the electrode layers was also demonstrated with a commercial PEDOT electrode, which exhibited convincing results up to 50% strain. As such, it can be concluded that the stretchability and light-emitting properties of the ACEL device are contingent upon the stretchability and conductivity of the RBM film. As showcased in Fig. 6D (top), in its original state, the ACEL device displayed a uniform, bright blue light emission across the entire emission layer. The device maintained uniform light emission until the strain reached 20%, which was the elongation at break of the RBM film (Fig. 5A). It is notable that the ACEL device was unable to withstand further stretching beyond 20% due to the fracture of the RBM film.

Moreover, the luminescence stability of the ACEL device under stretching was monitored as displayed in Fig. 6E. The observed change in luminance may be attributed to a combination of factors, including the thickness variation in the emission layer and the conductivity alteration in the RBM electrode. In the case of smaller stretching strains (up to 5%), the reduction in thickness of the emission layer caused an increase in the electrical field surrounding the ZnS nanoparticles (50). Concurrently, the conductivity of the RBM film electrode shows a slight enhancement, as can be referred to Fig. 6A. Both of these factors contributed to the observed rise in luminance (Fig. 6E). However, when the stretching strain exceeded 10%, the reduction in ZnS nanoparticle density and the elevated resistance of the RBM films resulted in a decline in luminance (Fig. 6E). Besides, on the basis of the mechanical robustness and stable conductivity of the RBM film electrode, the ACEL devices were patternable when the PEDOT electrode was replaced with a Ag nanowire (AgNW) electrode because AgNWs were easier to pattern than PEDOT (see Materials and Methods). As presented in Fig. 6D (bottom) and fig. S16, the ACEL devices were successfully patterned into “SJTU” letters, flower, tree, moon, and star shapes. Therefore, the results demonstrate that the stretchable and patterned ACEL devices with high brightness and uniform light emission can be manufactured using RBM electrodes.

### DISCUSSION

In summary, we have developed stretchable and patternable ACEL devices based on the RBM film electrodes, which were fabricated by bridging MXene platelets with [2]rotaxane through the formation of covalent carbonate ester linkage. In response to external forces, the intramolecular motion of [2]rotaxane likely facilitates the release of hidden chain, thereby increasing the slip distance between MXene platelets. Consequently, the incorporation of [2]rotaxane markedly enhanced the mechanical properties of RBM films. The results demonstrated that RBM films achieved a maximum strain of 20.0% and a high toughness of  $11.9 \text{ MJ/m}^3$  with only 3.6% [2]rotaxane by weight, which are the maximum attainable level with no more than 5 wt % additives. In addition, the interplanar spacing of RBM films remained largely unchanged despite the introduction of [2]rotaxane. Furthermore, the RBM films showed consistent and reversible resistance alterations when cyclically stretched 500 times in the strain range between 0 and 15%. Benefiting from the mechanical robustness and stable conductivity, the RBM films enabled the fabrication of stretchable ACEL devices, customizable with various patterns. Our work not only develops an accessible and effective approach for assembling high-performance two-dimensional material films but also opens exciting possibilities for applications in stretchable electronic devices, offering substantial promise and potential.

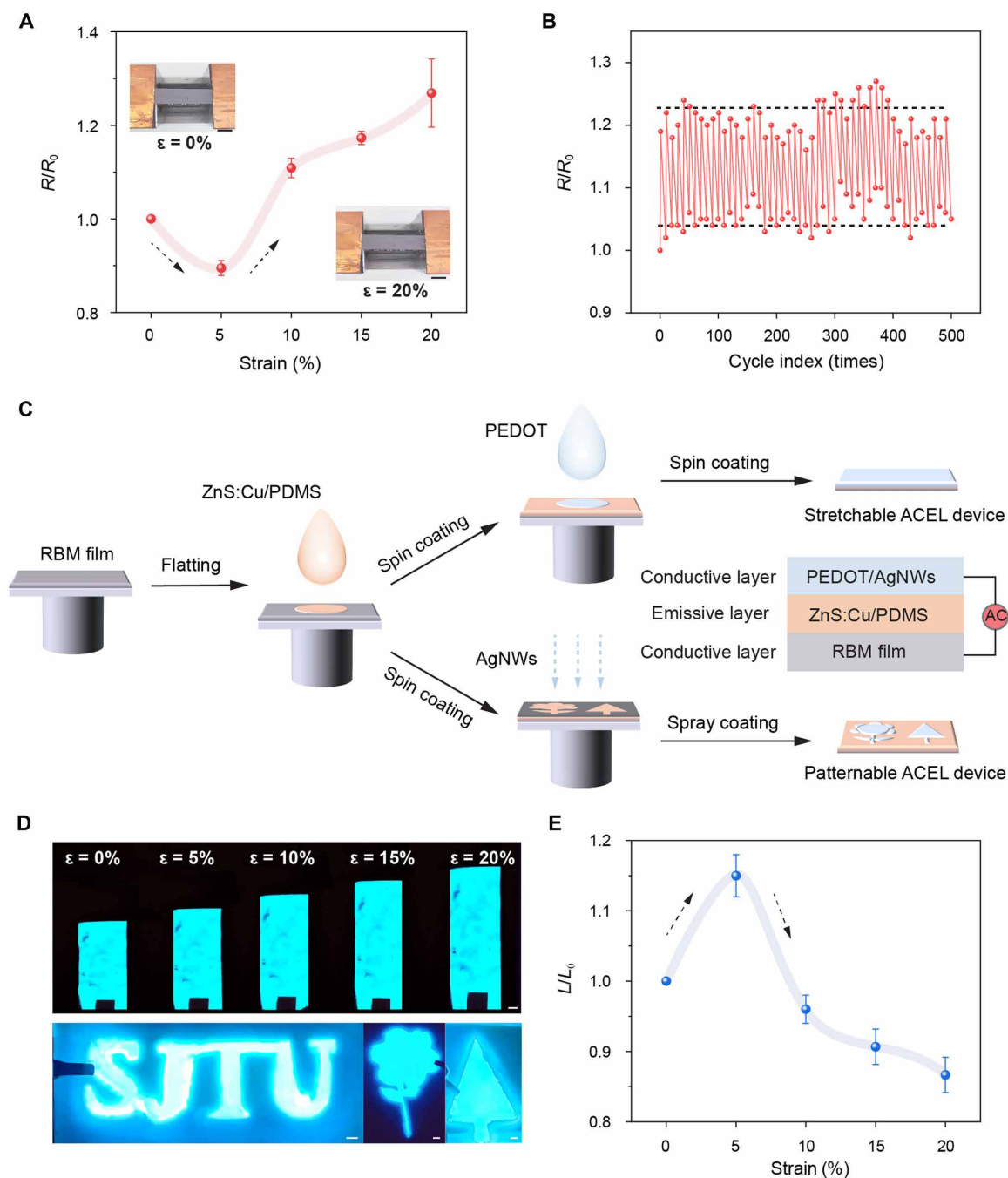


**Fig. 6. Application of RBM films as stretchable electrodes for ACEL devices.** (A) Relative resistance changes of the RBM films under tensile strain up to 20% (inset: digital photographs of the RBM film during a stretching test from initial state to 20% strain,  $\epsilon$ : elongation). Scale bars, 1 cm.  $R_0$  and  $R$  represent the resistance of the RBM film before and after being stretched, respectively. (B) Relative resistance changes of the RBM films under cyclic stretching tests between 0 and 15% strain for 500 cycles. (C) Diagram showing the fabrication process of ACEL devices. First, RBM film is flattened on a glass substrate, and then ZnS:Cu/PDMS layer is spin-coated onto the RBM film. To obtain stretchable ACEL device, spin coating is used to make a PEDOT layer. By contrast, a patternable ACEL device is prepared by spray coating AgNW solution onto the PET shadow mask covering the ZnS:Cu/PDMS layer. Hence, the emissive layer is excited by connecting the conductive layers with an alternate current, resulting in the illuminated ACEL devices. (D) Top: Digital photographs of the ACEL device under stretching strains of 0, 5, 10, 15, and 20%, respectively. Scale bar, 1 mm. Bottom: Digital photographs of patterned ACEL devices showing SJTU letters, flower, and tree shapes. Scale bars, 2 mm. (E) Dependence of relative luminance of a stretchable ACEL device with different strains.  $L_0$  and  $L$  represent the luminance before and after the ACEL device was stretched, respectively.

## MATERIALS AND METHODS

### Materials

All reagents were commercially available in Reagent Grade and used as supplied without further purification. Titanium aluminium carbide ( $\text{Ti}_3\text{AlC}_2$ , 400 mesh) was supplied by Jilin 11 Technology Co. Ltd. Hydrochloric acid (HCl, 36.0 to 38.0%) was provided by Sino-pharm Chemical Reagent Co. Ltd. PDMS base and curing agent were purchased from Dow Corning. ZnS:Cu phosphor microparticles were procured from Lonco Co. Ltd. PEDOT transparent conductive ink was obtained from Shenzhen Yilai Technology Co. Ltd. AgNWs (AW045) as suspensions in water were purchased from Zhejiang Kechuang Advanced Materials.

### Synthesis of titanium carbide ( $\text{Ti}_3\text{C}_2\text{T}_x$ )

$\text{Ti}_3\text{C}_2\text{T}_x$  MXene was prepared by etching  $\text{Ti}_3\text{AlC}_2$  according to the MILD method (32). In detail, lithium fluoride (0.8 g) was firstly mixed with hydrochloric acid (HCl, 10 ml, 9 M) in a Teflon vessel by stirring for several minutes. Second,  $\text{Ti}_3\text{AlC}_2$  powder (0.5 g) was slowly added within several minutes, and then the stirring was kept for 24 hours at 30°C. Next, the mixture was washed at least four times using deionized water (DIW) by centrifugation at 3500 rpm for 5 min until the pH of supernatant was near-neutral (more than 6). Afterward, the collected sediment was dispersed with a certain volume of DIW, followed by ultrasonic ice bath for 45 min. Last, the MXene dispersion was acquired by centrifugation at 4000 rpm for 8 min to collect the supernatant.

### Synthesis of [2]rotaxane decorated by carbonyl imidazole unit ([2]rotaxane-CDI)

First, [2]rotaxane terminated with two —OH groups was obtained according to our previous report (28). Then, the [2]rotaxane (0.1 g, 0.07 mmol) reacted with an excess CDI (0.3 g, 1.9 mmol) in dichloromethane (DCM; 5 ml) by stirring for 24 hours at 25°C. In the next step, the DCM solution was extracted with 100 ml water for three times and one more time using saturated brine. In the last, the rotary evaporator was carried out to remove DCM to get [2]rotaxane-CDI. Meanwhile, heptaethylene glycol was also reacted with CDI to replace —OH groups with carbonyl imidazole units (heptaethylene glycol-CDI).

### Fabrication of RBM films

Five milliliters of MXene dispersion (5 mg/ml) obtained above was vacuum suction onto the hydrophilic filter membrane. After a period of natural drying, MXene films (~25 mg) were separated from the hydrophilic filter membrane. Subsequently, MXene films were immersed in *N,N*-dimethylformamide (5 ml), and [2]rotaxane-CDI (10 mg, 0.007 mmol) was added immediately at 45°C. Until 12 hours later, MXene films were rinsed by ethanol for five times to get rid of unreacted [2]rotaxane-CDI. RBM films were obtained after vacuum drying overnight at 45°C. As control, HBM films were also prepared using the same method.

### Fabrication of stretchable ACEL devices

The ACEL devices were prepared by spin coating. A precleaned glass was used as the substrate, the RBM film and the PEDOT electrode were used as the bottom and top electrodes, respectively. ZnS:Cu/PDMS was used as the emissive layer. The ZnS:Cu/PDMS composite was prepared by mixing ZnS:Cu microparticles (4 g) and PDMS (2 g, the weight ratio of base and curing agents was 10:1) in a speed mixer at 2500 rpm for 5 min.

Before spin coating, the RBM films were flattened on glass substrate and affixed with a double-sided tape (3M 55236) to prevent wrinkling during coating process. The ZnS:Cu/PDMS composite was then dropped onto the RBM film and spread evenly with a glass rod. Immediately, the ZnS:Cu/PDMS composite was spin-coated at a spin speed of 3000 rpm, with an acceleration of 1500 rpm/s for 30 s. Subsequently, the ZnS:Cu/PDMS-coated RBM film was thermally cured at 80°C for 1 hour. Next, the top electrode of PEDOT layer was spin-coated at a spin speed of 2000 rpm, with an acceleration of 1000 rpm/s for 30 s. Thereafter, the entire device was subjected to thermal annealing on a hot plate at 100°C for 15 min. Last, copper foils were connected to the top and bottom electrode layers. The ACEL device was illuminated by an input power of 100V AC.

### Fabrication of patterned ACEL devices

The fabrication process of RBM electrodes and ZnS:Cu/PDMS emissive layers was mentioned above. However, the top PEDOT electrode was replaced with AgNWs because PEDOT is unsuitable for patterning, whereas AgNWs can be perfectly tailored to the desired patterns. To this end, shadow masks with different shapes were fabricated using polyethylene terephthalate (PET) films. The AgNWs solutions (0.5 mg/ml in isopropanol) were then spray-coated on to the ZnS:Cu/PDMS layer through the shadow masks with the desired patterns under a hot plate at 115°C. By doing so, the patterned ACEL devices were obtained. Last, copper foils were connected to the top and bottom electrode layers, and the patterned ACEL devices were illuminated by an input power of 100V AC.

### Supplementary Materials

#### This PDF file includes:

Supplementary Text  
Figs. S1 to S18  
Tables S1 and S2  
References

### REFERENCES AND NOTES

- M. Naguib, M. Kurtoglu, V. Presser, J. Lu, J. Niu, M. Heon, L. Hultman, Y. Gogotsi, M. W. Barsoum, Two-dimensional nanocrystals produced by exfoliation of  $\text{Ti}_3\text{AlC}_2$ . *Adv. Mater.* **23**, 4248–4253 (2011).
- B. Anasori, M. R. Lukatskaya, Y. Gogotsi, 2D metal carbides and nitrides (MXenes) for energy storage. *Nat. Rev. Mater.* **2**, 16098 (2017).
- A. VahidMohammadi, J. Rosen, Y. Gogotsi, The world of two-dimensional carbides and nitrides (MXenes). *Science* **372**, eabf1581 (2021).
- W. Tian, A. VahidMohammadi, M. S. Reid, Z. Wang, L. Ouyang, J. Erlandsson, T. Pettersson, L. Wågberg, M. Beidaghi, M. M. Hamed, Multifunctional nanocomposites with high strength and capacitance using 2D MXene and 1D nanocellulose. *Adv. Mater.* **31**, e1902977 (2019).
- X. Gao, X. Du, T. S. Mathis, M. Zhang, X. Wang, J. Shui, Y. Gogotsi, M. Xu, Maximizing ion accessibility in MXene-knotted carbon nanotube composite electrodes for high-rate electrochemical energy storage. *Nat. Commun.* **11**, 6160 (2020).
- X. Li, Z. Huang, C. E. Shuck, G. Liang, Y. Gogotsi, C. Zhi, MXene chemistry, electrochemistry and energy storage applications. *Nat. Rev. Chem.* **6**, 389–404 (2022).
- R. Qin, J. Nong, K. Wang, Y. Liu, S. Zhou, M. Hu, H. Zhao, G. Shan, Recent advances in flexible pressure sensors based on MXene materials. *Adv. Mater.* **36**, e2312761 (2024).
- J. Lipton, J. A. Röhr, V. Dang, A. Goad, K. Maleski, F. Lavini, M. Han, E. H. R. Tsai, G.-M. Weng, J. Kong, E. Riedo, Y. Gogotsi, A. D. Taylor, Scalable, highly conductive, and micropatternable MXene films for enhanced electromagnetic interference shielding. *Matter* **3**, 546–557 (2020).
- W. Li, T. Zhou, Z. Zhang, L. Li, W. Lian, Y. Wang, J. Lu, J. Yan, H. Wang, L. Wei, Q. Cheng, Ultrastrong MXene film induced by sequential bridging with liquid metal. *Science* **385**, 62–68 (2024).
- Z. Ling, C. E. Ren, M.-Q. Zhao, J. Yang, J. M. Giammarco, J. Qiu, M. W. Barsoum, Y. Gogotsi, Flexible and conductive MXene films and nanocomposites with high capacitance. *Proc. Natl. Acad. Sci. U.S.A.* **111**, 16676–16681 (2014).

11. Z. Zhang, S. Yang, P. Zhang, J. Zhang, G. Chen, X. Feng, Mechanically strong MXene/Kevlar nanofiber composite membranes as high-performance nanofluidic osmotic power generators. *Nat. Commun.* **10**, 2920 (2019).
12. L. Ding, L. Li, Y. Liu, Y. Wu, Z. Lu, J. Deng, Y. Wei, J. Caro, H. Wang, Effective ion sieving with  $\text{Ti}_3\text{C}_2\text{T}_x$  MXene membranes for production of drinking water from seawater. *Nat. Sustain.* **3**, 296–302 (2020).
13. Y. Deng, T. Shang, Z. Wu, Y. Tao, C. Luo, J. Liang, D. Han, R. Lyu, C. Qi, W. Lv, F. Kang, Q. H. Yang, Fast gelation of  $\text{Ti}_3\text{C}_2\text{T}_x$  MXene initiated by metal ions. *Adv. Mater.* **31**, 1902432 (2019).
14. G. S. Lee, T. Yun, H. Kim, I. H. Kim, J. Choi, S. H. Lee, H. J. Lee, H. S. Hwang, J. G. Kim, D.-W. Kim, H. M. Lee, C. M. Koo, S. O. Kim, Mussel inspired highly aligned  $\text{Ti}_3\text{C}_2\text{T}_x$  MXene film with synergistic enhancement of mechanical strength and ambient stability. *ACS Nano* **14**, 11722–11732 (2020).
15. J. Shen, G. Liu, Y. Ji, Q. Liu, L. Cheng, K. Guan, M. Zhang, G. Liu, J. Xiong, J. Yang, W. Jin, 2D MXene nanofilms with tunable gas transport channels. *Adv. Funct. Mater.* **28**, 1801511 (2018).
16. S. Wan, X. Li, Y. Chen, N. Liu, Y. Du, S. Dou, L. Jiang, Q. Cheng, High-strength scalable MXene films through bridging-induced densification. *Science* **374**, 96–99 (2021).
17. S. Wan, X. Li, Y. Wang, Y. Chen, X. Xie, R. Yang, A. P. Tomsia, L. Jiang, Q. Cheng, Strong sequentially bridged MXene sheets. *Proc. Natl. Acad. Sci. U.S.A.* **117**, 27154–27161 (2020).
18. Z. Liu, Y. Zhang, H.-B. Zhang, Y. Dai, J. Liu, X. Li, Z.-Z. Yu, Electrically conductive aluminum ion-reinforced MXene films for efficient electromagnetic interference shielding. *J. Mater. Chem. C* **8**, 1673–1678 (2020).
19. Y. Zhu, Y. Xia, M. Wu, W. Guo, C. Jia, X. Wang, Wearable, freezing-tolerant, and self-powered electroluminescence system for long-term cold-resistant displays. *Nano Energy* **98**, 107309 (2022).
20. Y. Xia, Y. Zhu, X. Zhi, W. Guo, B. Yang, S. Zhang, M. Li, X. Wang, C. Pan, Transparent self-healing anti-freezing ionogel for monolayered triboelectric nanogenerator and electromagnetic energy-based touch panel. *Adv. Mater.* **36**, 2308424 (2023).
21. D. Sluysmans, J. F. Stoddart, The burgeoning of mechanically interlocked molecules in chemistry. *Trends Chem.* **1**, 185–197 (2019).
22. M. R. Wilson, J. Solà, A. Carlone, S. M. Goldup, N. Lebrasseur, D. A. Leigh, An autonomous chemically fuelled small-molecule motor. *Nature* **534**, 235–240 (2016).
23. R. Bai, Z. Zhang, W. Di, X. Yang, J. Zhao, H. Ouyang, G. Liu, X. Zhang, L. Cheng, Y. Cao, W. Yu, X. Yan, Oligo[2]catenane that is robust at both the microscopic and macroscopic scales. *J. Am. Chem. Soc.* **145**, 9011–9020 (2023).
24. W. Wang, S. Zhou, X. Yu, Q.-H. Guo, Y. Ma, J. Song, L. Zhang, X. Yan, L. Han, Q. Liao, X. Li, W.-B. Zhang, Y. Mai, S. Zhang, S. Che, H.-B. Yang, X. Fu, M.-X. Wang, What can topology bring to chemistry? *CCS Chem.* **6**, 2084–2109 (2024).
25. Y. Wang, L. Yang, L. Cheng, J. Zhao, R. Bai, W. Wang, S. Qu, Z. Zhang, W. Yu, X. Yan, Strengthening and toughening styrene-butadiene rubber by mechanically interlocked cross-links. *Sci. China: Chem.* **67**, 3414–3422 (2024).
26. B. Lee, Z. Niu, S. L. Craig, The mechanical strength of a mechanical bond: Sonochemical polymer mechanochemistry of poly(catenane) copolymers. *Angew. Chem. Int. Ed. Engl.* **55**, 13086–13089 (2016).
27. G. De Bo, Mechanochemistry of the mechanical bond. *Chem. Sci.* **9**, 15–21 (2018).
28. X. Yang, L. Cheng, Z. Zhang, J. Zhao, R. Bai, Z. Guo, W. Yu, X. Yan, Amplification of integrated microscopic motions of high-density [2]rotaxanes in mechanically interlocked networks. *Nat. Commun.* **13**, 6654 (2022).
29. C. J. Bruns, J. F. Stoddart, Rotaxane-based molecular muscles. *Acc. Chem. Res.* **47**, 2186–2199 (2014).
30. C. Wang, B. Gao, F. Fang, W. Qi, G. Yan, J. Zhao, W. Wang, R. Bai, Z. Zhang, Z. Zhang, W. Zhang, X. Yan, A stretchable and tough graphene film enabled by mechanical bond. *Angew. Chem. Int. Ed. Engl.* **63**, e202404481 (2024).
31. J. Zhao, Z. Zhang, C. Wang, X. Yan, Synergistic dual dynamic bonds in covalent adaptable networks. *CCS Chem.* **6**, 41–56 (2024).
32. Y. Jiang, Z. Zhang, Y.-X. Wang, D. Li, C.-T. Coen, E. Hwaun, G. Chen, H.-C. Wu, D. Zhong, S. Niu, W. Wang, A. Saberi, J.-C. Lai, Y. Wu, Y. Wang, A. A. Trotsyuk, K. Y. Loh, C.-C. Shih, W. Xu, K. Liang, K. Zhang, Y. Bai, G. Gurusankar, W. Hu, W. Jia, Z. Cheng, R. H. Dauskardt, G. C. Gurtner, J. B. H. Tok, K. Deisseroth, I. Soltész, Z. Bao, Topological supramolecular network enabled high-conductivity, stretchable organic bioelectronics. *Science* **375**, 1411–1417 (2022).
33. J. Gu, F. Li, Y. Zhu, D. Li, X. Liu, B. Wu, H. A. Wu, X. Fan, X. Ji, Y. Chen, J. Liang, Extremely robust and multifunctional nanocomposite fibers for strain-unperturbed textile electronics. *Adv. Mater.* **35**, e2209527 (2023).
34. M. Alhabeb, K. Maleski, B. Anasori, P. Lelyukh, L. Clark, S. Sin, Y. Gogotsi, Guidelines for synthesis and processing of two-dimensional titanium carbide ( $\text{Ti}_3\text{C}_2\text{T}_x$  MXene). *Chem. Mater.* **29**, 7633–7644 (2017).
35. T. Zhou, Y. Yu, B. He, Z. Wang, T. Xiong, Z. Wang, Y. Liu, J. Xin, M. Qi, H. Zhang, X. Zhou, L. Gao, Q. Cheng, L. Wei, Ultra-compact MXene fibers by continuous and controllable synergy of interfacial interactions and thermal drawing-induced stresses. *Nat. Commun.* **13**, 4564 (2022).
36. L. Ding, Y. Wei, L. Li, T. Zhang, H. Wang, J. Xue, L.-X. Ding, S. Wang, J. Caro, Y. Gogotsi, MXene molecular sieving membranes for highly efficient gas separation. *Nat. Commun.* **9**, 155 (2018).
37. J. Yan, T. Zhou, X. Yang, Z. Zhang, L. Li, Z. Zou, Z. Fu, Q. Cheng, Strong and tough MXene bridging-induced conductive nacre. *Angew. Chem. Int. Ed. Engl.* **63**, e202405228 (2024).
38. J. Zhao, F. Gao, S. P. Pujari, H. Zuilhof, A. V. Tpeplyakov, Universal calibration of computationally predicted N 1s binding energies for interpretation of XPS experimental measurements. *Langmuir* **33**, 10792–10799 (2017).
39. J. S. Stevens, S. J. Byard, C. C. Seaton, G. Sadiq, R. J. Davey, S. L. M. Schroeder, Proton transfer and hydrogen bonding in the organic solid state: A combined XRD/XPS/ssNMR study of 17 organic acid-base complexes. *Phys. Chem. Chem. Phys.* **16**, 1150–1160 (2014).
40. S. Wan, Y. Chen, S. Fang, S. Wang, Z. Xu, L. Jiang, R. H. Baughman, Q. Cheng, High-strength scalable graphene sheets by freezing stretch-induced alignment. *Nat. Mater.* **20**, 624–631 (2021).
41. S. Wan, Y. Li, J. Mu, A. E. Aliev, S. Fang, N. A. Kotov, L. Jiang, Q. Cheng, R. H. Baughman, Sequentially bridged graphene sheets with high strength, toughness, and electrical conductivity. *Proc. Natl. Acad. Sci. U.S.A.* **115**, 5359–5364 (2018).
42. S. Wan, X. Li, Y. Chen, N. Liu, S. Wang, Y. Du, Z. Xu, X. Deng, S. Dou, L. Jiang, Q. Cheng, Ultrastrong MXene films via the synergy of intercalating small flakes and interfacial bridging. *Nat. Commun.* **13**, 7340 (2022).
43. S. Ahn, T. H. Han, K. Maleski, J. Song, Y. H. Kim, M. H. Park, H. Zhou, S. Yoo, Y. Gogotsi, T. W. Lee, A 2D titanium carbide MXene flexible electrode for high-efficiency light-emitting diodes. *Adv. Mater.* **32**, e2000919 (2020).
44. H. Zhou, S. J. Han, H. D. Lee, D. Zhang, M. Anayee, S. H. Jo, Y. Gogotsi, T. W. Lee, Overcoming the limitations of MXene electrodes for solution-processed optoelectronic devices. *Adv. Mater.* **34**, e2206377 (2022).
45. B. Lyu, M. Kim, H. Jing, J. Kang, C. Qian, S. Lee, J. H. Cho, Large-area MXene electrode array for flexible electronics. *ACS Nano* **13**, 11392–11400 (2019).
46. S. Zhang, Y. Zhu, Y. Xia, K. Liu, S. Li, B. Yang, M. Li, X. Zhi, X. Wang, Wearable integrated self-powered electroluminescence display device based on all-in-one MXene electrode for information encryption. *Adv. Funct. Mater.* **33**, 2307609 (2023).
47. J. Wang, C. Yan, K. J. Chee, P. S. Lee, Highly stretchable and self-deformable alternating current electroluminescent devices. *Adv. Mater.* **27**, 2876–2882 (2015).
48. F. Stauffer, K. Tybrandt, Bright stretchable alternating current electroluminescent displays based on high permittivity composites. *Adv. Mater.* **28**, 7200–7203 (2016).
49. H. Dinh Xuan, B. Timothy, H. Y. Park, T. N. Lam, D. Kim, Y. Go, J. Kim, Y. Lee, S. I. Ahn, S. H. Jin, J. Yoon, Super stretchable and durable electroluminescent devices based on double-network ionogels. *Adv. Mater.* **33**, e2008849 (2021).
50. Y. J. Tan, H. Godaba, G. Chen, S. T. M. Tan, G. Wan, G. Li, P. M. Lee, Y. Cai, S. Li, R. F. Shepherd, J. S. Ho, B. C. K. Tee, A transparent, self-healing and high- $\kappa$  dielectric for low-field-emission stretchable optoelectronics. *Nat. Mater.* **19**, 182–188 (2020).
51. J. Liu, Z. Liu, H.-B. Zhang, W. Chen, Z. Zhao, Q.-W. Wang, Z.-Z. Yu, Ultrastrong and highly conductive MXene-based films for high-performance electromagnetic interference shielding. *Adv. Electron. Mater.* **6**, 1901094 (2019).
52. H. Chen, Y. Wen, Y. Qi, Q. Zhao, L. Qu, C. Li, Pristine titanium carbide MXene films with environmentally stable conductivity and superior mechanical strength. *Adv. Funct. Mater.* **30**, 1906996 (2019).
53. J. Zhang, N. Kong, S. Uzun, A. Levitt, S. Seyedin, P. A. Lynch, S. Qin, M. Han, W. Yang, J. Liu, X. Wang, Y. Gogotsi, J. M. Razal, Scalable manufacturing of free-standing, strong  $\text{Ti}_3\text{C}_2\text{T}_x$  MXene films with outstanding conductivity. *Adv. Mater.* **32**, 2001093 (2020).

#### Acknowledgments

**Funding:** X.Y. acknowledges the financial support of the NSFC/China (22471164, 52421006, 22122105, and 22071152), the NSF of Shanghai (22dz1207603), the Shuguang Program of Shanghai Education Development Foundation and Shanghai Municipal Education Commission (22SG11), and the Starry Night Science Fund of Zhejiang University Shanghai Institute for Advanced Study (SN-ZJU-SIAS-006). Zhitao Zhang acknowledges the financial support of the NSFC/China (BE1100046 and 52473183), National Key R&D Program of China (2023YFA0915200), and Shanghai Science and Technology Innovation Action Plan Project (23JC1402900). Zhaoming Zhang acknowledges the financial support of the NSFC/China (22101175 and 22475128). R.B. acknowledges the financial support of the NSFC/China (22401185). **Author contributions:** Conceptualization: C.W. and X.Y. Methodology: C.W. and B.G. Visualization: C.W., W.W., and J.Z. Investigation: K.X., R.B., T.Y., Z.F., M.Y., and Zhaoming Zhang. Supervision: X.Y. and Zhitao Zhang. Writing—original draft: C.W. and B.G. Writing—review and editing: C.W. and X.Y. **Competing interests:** C.W. and X.Y. are coapplicants of a pending patent (application number CN202411460934.3, filed 18 October 2024) related to the technology used in this study and filed at the China National Intellectual Property Administration. The other authors declare that they have no competing interests. **Data and materials availability:** All data needed to evaluate the conclusions in the paper are present in the paper and/or the Supplementary Materials.

Submitted 13 October 2024

Accepted 31 January 2025

Published 7 March 2025

10.1126/sciadv.adt8262